Water, Not Salt, Causes Most of the Seebeck Effect of Nonisothermal Aqueous Electrolytes

Ole Nickel,[1] Ludwig J. V. Ahrens-Iwers,[2] Robert H. Meißner,[1,3,*] and Mathijs Janssen[4,†]
[1]Institute of Polymers and Composites, Hamburg University of Technology, Hamburg, Germany
[2]Institute of Advanced Ceramics, Hamburg University of Technology, Hamburg, Germany
[3]Institute of Surface Science, Helmholtz-Zentrum Hereon, Geesthacht, Germany
[4]Norwegian University of Life Sciences, Faculty of Science and Technology, Ås, Norway

(Received 6 September 2023; revised 5 December 2023; accepted 1 April 2024; published 29 April 2024)

A temperature difference between two electrolyte-immersed electrodes often yields a voltage $\Delta\psi$ between them. This electrolyte Seebeck effect is usually explained by cations and anions flowing differently in thermal gradients. However, using molecular simulations, we found almost the same $\Delta\psi$ for cells filled with pure water as with aqueous alkali halides. Water layering and orientation near polarizable electrodes cause a large temperature-dependent potential drop χ there. The difference in χ of hot and cold electrodes captures most of the thermovoltage, $\Delta\psi \approx \chi_{\mathrm{hot}} - \chi_{\mathrm{cold}}$.

DOI: 10.1103/PhysRevLett.132.186201

Industries discard thermal energy on a large scale, and tapping into this resource may help society with its much-needed energy transition [1]. Among the alternatives, electric and electrochemical devices with temperature-induced open-circuit voltages are attractive, as they have no moving parts [2–4]. The generation of a thermovoltage $\Delta\psi = \psi_{\mathrm{hot}} - \psi_{\mathrm{cold}}$ by a device subject to a temperature difference $\Delta T = T_{\mathrm{hot}} - T_{\mathrm{cold}}$ is called the Seebeck effect, characterized by the Seebeck coefficient $\mathcal{S} = -\Delta\psi/\Delta T$ [3,5]. The Seebeck effect of solid-state devices relies on electrons and holes moving apart in thermal gradients [6]. Electrochemical cells filled with aqueous [7] and polymeric [8] electrolytes and ionic liquid–organic solvent mixtures [9,10] show a Seebeck effect as well, which is usually explained by anions and cations moving apart in thermal gradients. Faradaic processes can also cause a Seebeck effect in cells with redox-active electrolytes [5,11].

Ions move in nonisothermal fluids due to the interactions among themselves and with solvent molecules [4,12]. On mesoscopic length scales, the thermodiffusion flux of an ion species i can be written as $J_i^{\mathrm{th}} = -Q_i^* \nabla T$, with Q_i^* being the ions' heat of transport and T being temperature. The Q_i^* of aqueous electrolytes relate to the Gibbs free hydration energy G_i^{hyd} and hydration entropy S_i^{hyd} [13,14] by

$$\frac{Q_i^*}{T} = \frac{\mathrm{d}G_i^{\mathrm{hyd}}}{\mathrm{d}T} = -S_i^{\mathrm{hyd}}. \tag{1}$$

First, S_i^{hyd} is negative (and Q_i^* positive) for most ions, so when electrodes block fluxes, cations and anions pile up near the cold electrode. This so-called Soret effect of spatially varying salt concentration can be probed through its impact on the electrolyte's conductivity [15–17] and refractive index [18,19], giving experimental access to Q_i^*. Second, the size and valency of ions affect their hydration shell and, thus, their hydration entropy. According to Marcus's theory [20], smaller ions have larger hydration shells and more negative S_i^{hyd}. Third, Q_i^* tends to be larger for cations than for anions [21]. If so, thermodiffusion of an electrolyte between electrodes at different temperatures leads to excess cations near the cold and anions near the hot electrode. This charge separation causes a potential drop between the electrodes: the Seebeck effect. Combining J_i^{th} and the Nernst-Planck equation for ionic fluxes due to diffusion and electromigration, an expression can be derived for the steady-state Seebeck coefficient [7,18,22,23]. For binary electrolytes,

$$\mathcal{S} = \frac{Q_+^* - Q_-^*}{2eT}, \tag{2}$$

where e is the elementary charge. As Eq. (2) followed from an extended Nernst-Planck equation, it accounts for ionic thermodiffusion and mean-field electrostatic interactions. Finite ion sizes and ion-ion correlations, important for dense electrolytes and ionic liquids [24–26], are ignored, so Eq. (2) may not hold for such fluids.

Recent experiments on nonisothermal cells filled with aqueous [7] and polymeric [8] electrolytes found Seebeck coefficients above $\mathcal{S} = 1\ \mathrm{mV\,K^{-1}}$, much higher than predicted by Eq. (2). Another experiment found potential differences between blocking electrodes held at different

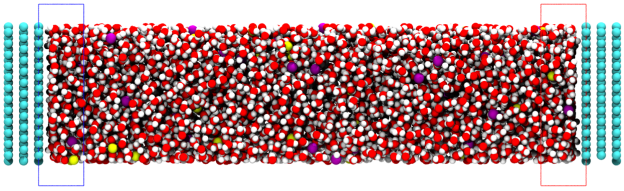

FIG. 1. Simulation snapshot of 1 M LiI in water between graphene electrodes. Thermostats control the temperature in the blue and red regions. (Li^+, yellow; I^-, purple; hydrogen, white; oxygen, red; carbon, cyan.)

temperatures in separate electrolyte reservoirs, ruling out thermodiffusion as its cause [27]. Together, these studies suggest that mechanisms beyond thermodiffusion contribute to the electrolyte Seebeck effect.

Molecular dynamics (MD) simulations may help identify these mechanisms. One study determined G_i^{hyd} from MD simulations of isothermal electrolytes at different temperatures [13]. Others simulated nonisothermal electrolytes [13,18,28] and found that the thermal polarization of bulk water contributes to the Seebeck effect [29]. However, all these studies simulated open, periodic systems without electrodes. Yet, the electrolyte-electrode interface may well contribute to the Seebeck effect. MD simulations of water-vapor interfaces revealed a potential drop χ over this interface of about -500 mV, varying with temperature by up to -1 mV/K [30–33]. If the surface potential at electrode-electrolyte interfaces also depends on temperature, holding two electrodes at different temperatures would produce different surface potentials and a potential difference between them. Here, we study nonisothermal thermoelectric cells with polarizable electrodes to determine how the electrode-electrolyte interface contributes to the electrolyte Seebeck effect.

We used the June 2022 version of LAMMPS [34] to perform MD simulations of water and aqueous CsF, KCl, NaCl, and LiI between two flat parallel blocking electrodes made from three graphene layers (see Fig. 1). The cell was in an open circuit configuration, and both electrodes were always overall charge neutral. Yet, the individual electrode atoms carried a fluctuating charge, in both space and time, as we treated graphene as a perfect conductor, hence, a constant-potential surface (in space, not in time). To simulate such electrodes, we used the constrained charge method [35] of the ELECTRODE package [36]. We used different force fields for the SPC/E water [37], graphene [38], and halide and alkali ions [39]. Nonbonded interactions had a cutoff of 1.2 nm, and the SHAKE algorithm held bonds and angles of water molecules rigid [40]. A PPPM k-space solver with a relative accuracy of 10^{-6} computed the long-range interactions [41]. The system was periodic in the electrode plane, and we modified the Ewald summation used to treat long-range electrostatics to account for slab geometries [42] and electrodes [41], removing interslab dipole interactions and effectively mimicking a two-dimensional periodic system. Initial simulation cells were around 3 nm × 3 nm × 16 nm. To adjust the electrolyte's density, we exerted a pressure of 1 bar on the left electrode through a 8.7 fN inward force on each of its atoms. After letting the system equilibrate for a few nanoseconds, the distance $2L$ between the electrodes was between 11.4 and 12.2 nm, and the position of the electrodes was fixed. Thermostats set the temperature of the electrolyte by global velocity rescaling with Hamiltonian dynamics [43] in two regions of width $\epsilon = 1$ nm next to the electrodes [44]. Upon applying a temperature difference ΔT, a linear temperature developed between the thermostats in less than 1 ns (see Fig. S3 in Supplemental Material [45]). All simulations were performed with a time step of 1 fs over 15 ns. For better statistics, simulations were repeated up to eight times with independent starting positions and flipped thermal gradients (thus, up to 16 simulations).

We first discuss cells with 3240 water molecules and no ions. We use a Cartesian coordinate system with x and y lying in the plane of the electrodes of surface area A; the coordinate z runs from $-L$ to L between the electrodes. The water's partial charges cause a spatially varying charge density $\rho(z)$ and local potential $\psi(z)$, according to the twice-integrated Poisson equation [29,30]

$$\psi(z) = -\frac{1}{\varepsilon_0}\int_{z_0}^{z}\int_{z_0}^{z'}\rho(z'')\mathrm{d}z''\mathrm{d}z', \tag{3}$$

where ε_0 is the vacuum permittivity and z_0 is an arbitrary reference point left of the cell where we set $\psi(z_0) = 0$. We sample $\rho(z)$ from the MD simulations by time averaging the partial charges in bins spanning the xy plane and 1 pm wide in the z direction.

Figure 2 shows $\psi(z)$ for a "cold" and "hot" isothermal system at 293 [Fig. 2(a)] and 373 K [Fig. 2(b)], respectively. In both panels, $\psi(z)$ varies strongly near the electrodes but not in the cell's interior. To characterize $\psi(z)$, we divide the cell into two interfacial regions $L - \delta < |z| < L$ of thickness δ and a bulk region where $|z| < L - \delta$. We choose δ so that the bulk region is $|z| < 4$ nm. From linear fits to the potential in the bulk $\psi_{\mathrm{fit}}(z)$, we determine the bulk potential drop $\Delta\psi_{\mathrm{bulk}} = \psi_{\mathrm{fit}}(L - \delta) - \psi_{\mathrm{fit}}(\delta - L)$. Both Figs. 2(a) and 2(b) have $\Delta\psi_{\mathrm{bulk}} \approx 0$ mV, so water molecules are not polarized in the bulk. We define the surface potential drop χ at each interface as the difference between the electrode potential and the average potential at the edge of the bulk region, $\chi_\pm = \psi_{\mathrm{fit}}(\pm L \mp \delta) - \psi(\pm L)$. We observe similar surface potentials at both electrodes $|\chi_-| \approx |\chi_+|$, with $\chi_{\mathrm{cold}} = -395$ mV and $\chi_{\mathrm{hot}} = -496$ mV. As a result, the potential difference $\Delta\psi = \psi(L) - \psi(-L)$ between electrodes, which can be partitioned as $\Delta\psi = \chi_- + \Delta\psi_{\mathrm{bulk}} - \chi_+$, is roughly zero. Figure S1 in Supplemental Material [45] shows that χ decreases roughly linearly between 293 and 373 K with $(\chi_{\mathrm{hot}} - \chi_{\mathrm{cold}})/80\ \mathrm{K} = -1.27$ mV/K, slightly higher than reported values for the SPC/E water-vapor interface [30,31].

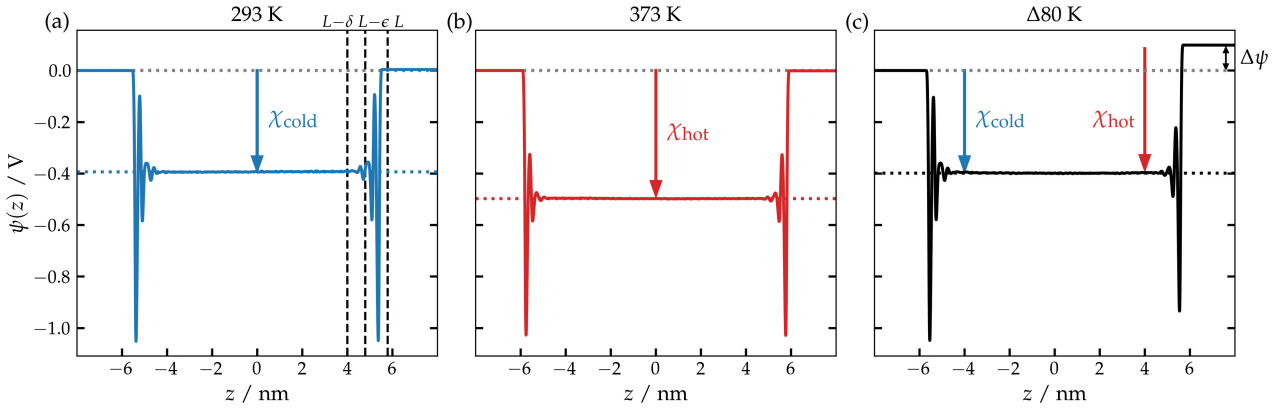

FIG. 2. Potential $\psi(z)$ in water-filled cells at 293 (a) and 373 K (b), and with a temperature gradient, where the left side is at 293 K and the right side is at 373 K (c).

Figure 2(c) shows $\psi(z)$ in a cell with electrodes held at 293 and 373 K, respectively. The respective surface potentials are similar to those in Figs. 2(a) and 2(b) and, therefore, depend on the *local* temperature: $\chi_- \approx \chi_{\text{cold}}$ and $\chi_+ \approx \chi_{\text{hot}}$. As the two surface potentials no longer cancel, $\Delta\psi$ is nonzero, and so is the associated Seebeck coefficient $\mathcal{S} = -1.26$ mV/K [47]. The nonisothermal cell also has a small bulk potential drop $\Delta\psi_{\text{bulk}} \approx 1$ mV, in line with previous MD studies [29,30,48,49]. To separate surface and bulk contributions to $\mathcal{S}$, we introduce a corresponding surface Seebeck coefficient $\mathcal{S}_{\text{surf}} = (\chi_+ - \chi_-)/\Delta T$ and bulk Seebeck coefficient $\mathcal{S}_{\text{bulk}} = -\Delta\psi_{\text{bulk}}/\Delta T_{\text{bulk}}$, where ΔT_{bulk} is the temperature drop over the bulk region, which we get from a linear fit to the temperature in that region; see Fig. S3 in Supplemental Material [45]. As $\Delta T_{\text{bulk}} < \Delta T$, these definitions yield $\mathcal{S} \neq \mathcal{S}_{\text{bulk}} + \mathcal{S}_{\text{surf}}$. Table I lists all the resulting coefficients.

Figure 3(a) shows the near-electrode potential profiles in Fig. 2(c) shifted to zero at the electrodes (dotted lines) and their underlying charge density profiles (solid lines). The peaks and valleys of the charge density are inversely related to those of the mass density (see Fig. S2 in Supplemental Material [45]): Where oxygen dominates, the charge density is negative and the mass density is high; where hydrogen dominates, the charge density is positive and the mass density is low. Figure 3 shows that the charge density $\rho(z)$ varies less at a higher temperature, changing the surface potential χ.

The usual approach to understanding the temperature-dependent surface potential drop of water is to insert multipole expansions of the charge density, $\rho(z) = \mathcal{M}(z) - (\mathrm{d}/\mathrm{d}z)\mathcal{P}_z(z) + (\mathrm{d}^2/\mathrm{d}^2 z)\mathcal{Q}_{zz}(z) + \cdots$, into Eq. (3) to determine how monopolar ($\mathcal{M}$), dipolar ($\mathcal{P}_z$), and quadrupolar ($\mathcal{Q}_{zz}$) terms contribute to $\psi(z)$ [29,30,32,48,50–57]. However, multipole expansions are not unique [58]: The terms $\mathcal{M}$, $\mathcal{P}_z$, and $\mathcal{Q}_{zz}$ contain an arbitrary reference point z_m^{ref} [see Eq. (S3) in Supplemental Material [45]]. Figure S5 in Supplemental Material [45] shows $\mathcal{P}_z$ and $\mathcal{Q}_{zz}$'s contributions to $\psi(z)$ for five different z_m^{ref} ($\mathcal{M} = 0$ for water). These data differ much, so the different terms in a multipole expansion give little physical insight. Nevertheless, $\mathcal{Q}_{zz}$'s contribution to the potential difference between two points is proportional to the difference in $\mathcal{Q}_{zz}(z)$ between those points [58]. As $\mathcal{Q}_{zz} = 0$ in the electrodes, the quadrupole density does not contribute to $\Delta\psi$. Consequently, in water-filled cells, only $\mathcal{P}_z$ (and $\mathcal{M}$, if ions are added) contribute to $\Delta\psi$.

To bypass the problems of multipole analyses, we introduce a method of quantifying water orientation near

TABLE I. Potential drop and Seebeck coefficients of water and several electrolytes in different cell regions (electrodes held at 293 and 373 K, respectively). Mean values and uncertainties are determined by block averaging 16 simulations.

	$\Delta\sigma_{\text{LJ}}$ (Å)	χ_- (mV)	$\Delta\psi_{\text{bulk}}$ (mV)	χ_+ (mV)	$\mathcal{S}$ (mV/K)	$\mathcal{S}_{\text{surf}}$ (mV/K)	$\mathcal{S}_{\text{bulk}}$ (mV/K)	$\mathcal{S}_{\text{Agar}}$ (mV/K)	$\mathcal{S}_{\text{Marcus}}$ (mV/K)
Water	⋯	-398 ± 2	1 ± 3	-498 ± 1	-1.26 ± 0.04	-1.25 ± 0.03	-0.01 ± 0.05	⋯[a]	⋯[a]
1 M CsF	0.08	-347 ± 6	-14 ± 11	-463 ± 5	-1.28 ± 0.11	-1.45 ± 0.12	0.23 ± 0.20	0.00	−0.40
1 M KCl	1.64	-391 ± 4	1 ± 7	-492 ± 4	-1.27 ± 0.09	-1.26 ± 0.06	-0.03 ± 0.11	0.03	−0.01
1 M NaCl	2.52	-422 ± 4	6 ± 13	-516 ± 4	-1.28 ± 0.14	-1.18 ± 0.06	-0.14 ± 0.22	0.05	0.19
1 M LiI	2.90	-416 ± 4	8 ± 6	-514 ± 5	-1.33 ± 0.07	-1.23 ± 0.07	-0.14 ± 0.11	0.03	0.55

[a]Agar, Mou, and Lin [21] reported Q_i^* and Marcus [20] S_i^{hyd} for OH^- and H_3O^+, but we did not include these ions in our MD simulations.

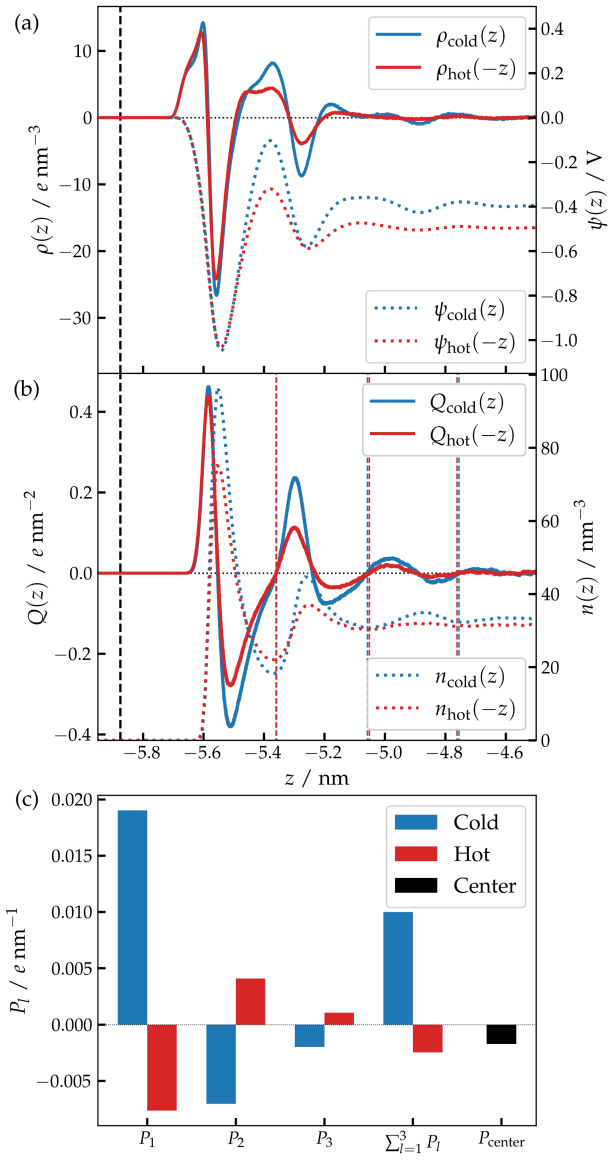

FIG. 3. Further analysis of the water-filled cell in Fig. 2(c) with temperature varying from 293 to 373 K. (a) Charge density and local potential, where the hot side at 373 K is mirrored around $z = 0$ and its potential in vacuum shifted to 0 V. The vertical black line indicates the position of the first graphene layer. (b) Cumulative charge (lines) and oxygen number density (dotted lines). (c) Layer dipole moment of water in the first three neutral layers near the cold and hot sides of the cell, their sum, and the dipole moment of the bulk water in the remainder of the cell (black).

electrodes, not relying on a molecular reference point. First, we compute the cumulative charge

$$Q(z) = \frac{1}{A}\int_{z_0}^{z} \mathrm{d}z' \sum_{i=1}^{N_a} \delta(z' - z_i) q_i \tag{4}$$

of N_a atoms with partial charge q_i and position z_i along the z axis. Figure 3(b) shows $Q(z)$ for the nonisothermal cell in Fig. 2(c). For a single layer of water molecules, seen as a peak in the oxygen density, $Q(z)$ rises, drops, passes zero, and rises again [59]. With the cumulative charge $Q(z)$, we can now identify water layers with no overall charge. These charge-neutral layers $l = 1, 2, 3, \ldots$ have boundaries ζ_{l-1} and ζ_l at the second crossings of the cumulative charge, $Q(\zeta_{l-1}) = Q(\zeta_l) = 0$; the first layer's boundary is at $\zeta_{l-1} = z_0$. With this definition, the layer boundaries (vertical dashed lines) are close to minima in the oxygen number density (dotted lines). Figure 3(b) clearly shows three layers near both electrodes; the boundaries of further layers are difficult to determine due to a weak signal-to-noise ratio. Accordingly, after the first three layers near both electrodes, the rest of the cell forms one big central layer. Finally, we characterize the distribution of atomic charges in layer l through its dipole

$$P_l = \frac{1}{A}\int_{\zeta_{l-1}}^{\zeta_l} \mathrm{d}z \sum_{i=1}^{N_a} \delta(z - z_i) z_i q_i. \tag{5}$$

The z_i values of the various atoms depend on one's choice of coordinate system. However, shifting the coordinate system $z \to z + \Delta z$ does not affect the layer dipole $P_l \to P_l + P_l'$, since $P_l' = (1/A)\Delta z \sum_{i \in l} q_i = 0$ for the uncharged layers. Figure 3(c) shows P_1, P_2, and P_3 on the cold (blue) and hot (red) sides of the cell in Fig. 2(c). P_l takes positive and negative values and has larger absolute values at the cold side. The figure also shows the sum of the dipoles, which is 3 times larger near the cold side, and the dipole moment P_{center} of the rest of the cell, which is much smaller than P_1 and P_2. Summing all P_l yields a nonzero overall dipole moment and associated potential drop $\Delta\psi = \sum_l P_l/\varepsilon_0$. Hence, Fig. 3(c) shows that an increase in temperature leads to decreased water ordering and, in turn, a net dipole and potential difference.

We now turn to electrolytes with 3240 water molecules and 58 ion pairs of CsF, KCl, NaCl, or LiI between electrodes held at 293 and 373 K. The ion's sizes are set by the $\sigma_{\mathrm{LJ}}^{\pm}$ parameter of the Lennard-Jones force field; Table I lists the differences in ion sizes $\Delta\sigma_{\mathrm{LJ}} = \sigma_{\mathrm{LJ}}^{-} - \sigma_{\mathrm{LJ}}^{+}$ for each electrolyte. The table also presents MD results for the different potential drops and Seebeck coefficients. Last, Table I contains predictions $\mathcal{S}_{\mathrm{Agar}}$ and $\mathcal{S}_{\mathrm{Marcus}}$, for which we inserted Q_i^* data from Table 1 of Agar, Mou, and Lin [21] and S_i^{hyd} data from Table 2 of Marcus [20] into Eqs. (1) and (2).

Table I shows us the following: First, our MD simulations yield negative $\mathcal{S}$ values similar to those of experiments on nanoporous carbon [27]. Experiments on titanium electrodes yielded positive $\mathcal{S}$ values instead [7]. This discrepancy may be caused by the different water structure near titanium, as the water layering depends strongly on the surface orientation and termination [60]. Second, Table I shows that $|\mathcal{S}| \gg |\mathcal{S}_{\mathrm{bulk}}|$ for all electrolytes, $|\mathcal{S}| \approx |\mathcal{S}_{\mathrm{surf}}|$ for most electrolytes, and adding ions to water

hardly affects $\mathcal{S}$. These observations suggest that the electrolyte Seebeck effect is more caused by interfacial electrolyte ordering than thermodiffusion. Third, for all ion pairs except CsF, $\mathcal{S}_{\mathrm{surf}}$ values lie around $\mathcal{S} = -1.26$ mV/K of pure water. This does not mean, however, that the electrolyte Seebeck effect is caused only by interfacial water structure. Adding ions to water changes χ_- and χ_+, but usually by the same amount, so the shifts in the surface potential drops cancel in $\mathcal{S}_{\mathrm{surf}} = (\chi_- - \chi_+)/\Delta T$. Figure S6 in Supplemental Material [45] suggests that the CsF anomaly is caused by a strong Cs^+ localization in the second water layer near the cold electrode, not present near the hot electrode. Fourth, $\mathcal{S}_{\mathrm{Agar}}$ and $\mathcal{S}_{\mathrm{Marcus}}$ correspond to bulk ionic thermodiffusion, but neither agrees with $\mathcal{S}_{\mathrm{bulk}}$. Marcus's theory predicts different-sized ions to have different S_i^{hyd}, so thermodiffusion should contribute strongly to the Seebeck coefficient of electrolytes with small and large ions [20]. We indeed see that $\mathcal{S}_{\mathrm{bulk}}$ decreases monotonically with $\Delta\sigma_{\mathrm{LJ}}$; Marcus's theory predicts a monotonic increase instead. The discrepancies between $\mathcal{S}_{\mathrm{bulk}}$ and $\mathcal{S}_{\mathrm{Agar}}$ and $\mathcal{S}_{\mathrm{Marcus}}$ may be caused by temperature and concentration dependence of $\mathcal{S}_{\mathrm{bulk}}$. Previous MD simulations found $\mathcal{S}_{\mathrm{bulk}}$ to depend strongly on temperature; for LiCl, $\mathcal{S}_{\mathrm{bulk}}$ changed sign around 305 K [29]. Moreover, Agar's and Marcus's data concerned electrolytes at infinite dilution, while our simulations discussed so far were at 1 M. In Supplemental Material [45] (see Fig. S7), we consider different salt concentrations and find that $\mathcal{S}_{\mathrm{bulk}}$ generally increases with concentration. However, even at the lowest concentrations of 0.5 M investigated, discrepancies between $\mathcal{S}_{\mathrm{bulk}}$ and $\mathcal{S}_{\mathrm{Agar}}$ and $\mathcal{S}_{\mathrm{Marcus}}$ persisted. Finally, the small values of $\mathcal{S}_{\mathrm{Agar}}$ and $\mathcal{S}_{\mathrm{Marcus}}$ further support our conclusion that the large $\mathcal{S}$ in our simulations cannot be explained by ionic thermodiffusion alone.

In summary, we presented the first MD simulations of nonisothermal electrolyte-filled cells with explicit electrodes. In our MD simulations, (i) the Seebeck effect of aqueous electrolytes is caused more by interfacial electrolyte structure than by ionic thermodiffusion; (ii) adding ions to pure water changes the interfacial electrolyte structure [61] but usually to the same degree near the cold and hot electrodes, leaving $\mathcal{S}_{\mathrm{surf}}$ unaffected; (iii) current models do not capture the thermodiffusion of dense electrolytes. Hence, further work is needed to fully understand the electrolyte Seebeck effect. So far, many experiments concerned polyelectrolytes, ionic polymer gels, and ionic liquids [4]. Experiments, theory, and simulations are more likely to meet for systems with simpler components, for instance, aqueous electrolytes, only a few of which have been studied [7]. Next, it would be interesting to go beyond our idealized flat-electrode setup. An electrode's shape, surface defects, and functional groups should affect the nearby electrolyte structure, so tailoring these properties could boost a system's Seebeck coefficient.

Funded by the Deutsche Forschungsgemeinschaft (DFG, German Research Foundation)—Project No. 192346071. M. J. was supported by a FRIPRO grant from The Research Council of Norway (Project No. 345079).

*robert.meissner@tuhh.de
†mathijs.a.janssen@nmbu.no

[1] H. Jouhara, N. Khordehgah, S. Almahmoud, B. Delpech, A. Chauhan, and S. A. Tassou, Thermal Sci. Eng. Prog. **6**, 268 (2018).
[2] H. Wang, D. Zhao, Z. U. Khan, S. Puzinas, M. P. Jonsson, M. Berggren, and X. Crispin, Adv. Electron. Mater. **3**, 1700013 (2017).
[3] B. Yang and G. Portale, Colloid Polym. Sci. **299**, 465 (2021).
[4] D. Zhao, A. Würger, and X. Crispin, J. Energy Chem. **61**, 88 (2021).
[5] M. F. Dupont, D. R. MacFarlane, and J. M. Pringle, Chem. Commun. (Cambridge) **53**, 6288 (2017).
[6] X. Zhang and L.-D. Zhao, J. Materiomics **1**, 92 (2015).
[7] A. L. Sehnem and M. Janssen, J. Chem. Phys. **154**, 164511 (2021).
[8] D. Zhao, H. Wang, Z. U. Khan, J. C. Chen, R. Gabrielsson, M. P. Jonsson, M. Berggren, and X. Crispin, Energy Environ. Sci. **9**, 1450 (2016).
[9] M. Bonetti, S. Nakamae, M. Roger, and P. Guenoun, J. Chem. Phys. **134**, 114513 (2011).
[10] M. Bonetti, S. Nakamae, B. T. Huang, T. J. Salez, C. Wiertel-Gasquet, and M. Roger, J. Chem. Phys. **142**, 244708 (2015).
[11] T. J. Abraham, D. R. MacFarlane, and J. M. Pringle, Chem. Commun. (Cambridge) **47**, 6260 (2011).
[12] S. Wiegand, J. Phys. Condens. Matter **16**, R357 (2004).
[13] L. Rezende Franco, A. L. Sehnem, A. M. Figueiredo Neto, and K. Coutinho, J. Chem. Theory Comput. **17**, 3539 (2021).
[14] N. Takeyama and K. Nakashima, J. Solution Chem. **17**, 305 (1988).
[15] D. G. Leaist and L. Hao, J. Chem. Soc., Faraday Trans. **90**, 1223 (1994).
[16] J. N. Agar and J. C. R. Turner, J. Phys. Chem. **64**, 1000 (1960).
[17] P. N. Snowdon and J. C. R. Turner, Trans. Faraday Soc. **56**, 1812 (1960).
[18] F. Römer, Z. Wang, S. Wiegand, and F. Bresme, J. Phys. Chem. B **117**, 8209 (2013).
[19] J. Colombani, H. Dez, J. Bert, and J. Dupuy-Philon, Phys. Rev. E **58**, 3202 (1998).
[20] Y. Marcus, Biophys. Chem. **51**, 111 (1994).
[21] J. N. Agar, C. Y. Mou, and J. L. Lin, J. Phys. Chem. **93**, 2079 (1989).
[22] E. D. Eastman, J. Am. Chem. Soc. **50**, 283 (1928).
[23] A. Würger, Rep. Prog. Phys. **73**, 126601 (2010).
[24] A. A. Kornyshev, J. Phys. Chem. B **111**, 5545 (2007).
[25] S. Kondrat, N. Georgi, M. V. Fedorov, and A. A. Kornyshev, Phys. Chem. Chem. Phys. **13**, 11359 (2011).
[26] S. S. Lee, A. Koishi, I. C. Bourg, and P. Fenter, Proc. Natl. Acad. Sci. U.S.A. **118**, e2105154118 (2021).

[27] B. Xu, L. Liu, H. Lim, Y. Qiao, and X. Chen, Nano Energy **1**, 805 (2012).
[28] S. Di Lecce, T. Albrecht, and F. Bresme, Sci. Rep. **7**, 44833 (2017).
[29] S. Di Lecce and F. Bresme, J. Phys. Chem. B **122**, 1662 (2018).
[30] A. Chapman and F. Bresme, Phys. Chem. Chem. Phys. **24**, 14924 (2022).
[31] S. M. Kathmann, I.-F. W. Kuo, C. J. Mundy, and G. K. Schenter, J. Phys. Chem. B **115**, 4369 (2011).
[32] V. P. Sokhan and D. J. Tildesley, Mol. Phys. **92**, 625 (1997).
[33] E. Harder and B. Roux, J. Chem. Phys. **129**, 234706 (2008).
[34] A. P. Thompson, H. M. Aktulga, R. Berger, D. S. Bolintineanu, W. M. Brown, P. S. Crozier, P. J. in 't Veld, A. Kohlmeyer, S. G. Moore, T. D. Nguyen, R. Shan, M. J. Stevens, J. Tranchida, C. Trott, and S. J. Plimpton, Comput. Phys. Commun. **271**, 108171 (2022).
[35] S. R. Tee and D. J. Searles, J. Chem. Theory Comput. **19**, 2758 (2023).
[36] L. J. V. Ahrens-Iwers, M. Janssen, S. R. Tee, and R. H. Meißner, J. Chem. Phys. **157**, 084801 (2022).
[37] H. J. C. Berendsen, J. R. Grigera, and T. P. Straatsma, J. Phys. Chem. **91**, 6269 (1987).
[38] A. Cheng and W. A. Steele, J. Chem. Phys. **92**, 3858 (1990).
[39] S. Deublein, J. Vrabec, and H. Hasse, J. Chem. Phys. **136**, 084501 (2012).
[40] J.-P. Ryckaert, G. Ciccotti, and H. J. C. Berendsen, J. Comput. Phys. **23**, 327 (1977).
[41] L. J. V. Ahrens-Iwers and R. H. Meißner, J. Chem. Phys. **155**, 104104 (2021).
[42] I.-C. Yeh and M. Berkowitz, J. Chem. Phys. **111**, 3155 (1999).
[43] G. Bussi, D. Donadio, and M. Parrinello, J. Chem. Phys. **126**, 014101 (2007).
[44] To corroborate this methodology with thermostats in the fluid, we performed simulations of water-filled cells where the temperature was applied to the electrodes instead. Both methods yielded the same $\mathcal{S}$ [45].
[45] See Supplemental Material at http://link.aps.org/supplemental/10.1103/PhysRevLett.132.186201 for additional analysis and figures, which includes Ref. [46].
[46] J. H. Los and A. Fasolino, Phys. Rev. B **68**, 024107 (2003).
[47] For nonisothermal systems with electrodes at temperatures between 293 and 373 K, we can estimate the surface potentials χ_{cold} and χ_{hot} and corresponding Seebeck coefficient $\approx\chi_{\mathrm{cold}}-\chi_{\mathrm{hot}}$ from an interpolation or fit to the χ of isothermal system plotted in Fig. S1 in Supplemental Material [45].
[48] J. Armstrong and F. Bresme, Phys. Rev. E **92**, 060103(R) (2015).
[49] Armstrong and Bresme [48] found strong water polarization at high temperatures (~550 K). The thermal polarization was much weaker in the liquid range of water, changing sign at 320 K.
[50] M. Matsumoto and Y. Kataoka, J. Chem. Phys. **88**, 3233 (1988).
[51] J. Glosli and M. Philpott, Electrochim. Acta **41**, 2145 (1996).
[52] D. J. Bonthuis, S. Gekle, and R. R. Netz, Langmuir **28**, 7679 (2012).
[53] J. R. Cendagorta and T. Ichiye, J. Phys. Chem. B **119**, 9114 (2015).
[54] I. Iriarte-Carretero, M. A. Gonzalez, J. Armstrong, F. Fernandez-Alonso, and F. Bresme, Phys. Chem. Chem. Phys. **18**, 19894 (2016).
[55] C. C. Doyle, Y. Shi, and T. L. Beck, J. Phys. Chem. B **123**, 3348 (2019).
[56] O. R. Gittus, P. Albella, and F. Bresme, J. Chem. Phys. **153**, 204503 (2020).
[57] M. R. Becker, P. Loche, and R. R. Netz, J. Chem. Phys. **157**, 240902 (2022).
[58] M. A. Wilson, A. Pohorille, and L. R. Pratt, J. Chem. Phys. **90**, 5211 (1989).
[59] For this analysis, we moved the two hydrogen atoms of each water molecule to the point between them. In this way, $Q(z)$ is a multiple of the oxygen charge, and the points where $Q(z)=0$ are easy to identify.
[60] G. Zhou, C. Liu, and L. Huang, J. Chem. Eng. Data **63**, 2420 (2018).
[61] J. G. Hedley, H. Berthoumieux, and A. A. Kornyshev, J. Phys. Chem. C **127**, 8429 (2023).